Mechanical Systems and Signal Processing 247 (2026) 113970

Contents lists available at ScienceDirect

Mechanical Systems and Signal Processing

journal homepage: www.elsevier.com/locate/ymssp

Full length article

Quantification and propagation of uncertainties in electroacoustic absorbers due to temperature effects using Bayesian inference

Leonardo Ferreira [a],*, Rafael Teloli [a], Emanuele De Bono [b], Morvan Ouisse [a]

[a] *Université Marie et Louis Pasteur, SUPMICROTECH, CNRS, institut FEMTO-ST, Besançon, 25000, France*
[b] *Università degli Studi di Napoli Federico II, Dipartimento di Ingegneria Industriale, Via Claudio 21, Naples, 80125, Italy*

ARTICLE INFO

Communicated by D. Yurchenko

Keywords:
Active noise control
Impedance control
Loudspeakers
Electroacoustic absorbers
Environmental effects
Uncertainty quantification
Bayesian inference
Affine invariant ensemble sampler
Thiele-Small parameters

ABSTRACT

Among technologies available for active noise control, electroacoustic absorbers (EAs) are devices whose acoustic impedance can be controlled to match a desired target value. This control depends on the electromechanical properties of the loudspeaker used in constructing the EA, known as Thiele-Small parameters. As these properties can be affected by environmental factors, such as temperature and humidity, uncertainties in the parameters of loudspeaker model can introduce uncertainty into the control law itself. This work proposes the quantification of the uncertainties in the Thiele-Small parameters of EAs due to temperature variations using a Bayesian inference framework, along with the propagation of these uncertainties to key operational metrics, namely the frequency response function (FRF) and the normal absorption coefficient. The acoustic impedance of multiple EAs is measured using an impedance tube over a broad temperature range, from −10 °C to +50 °C, and a pole-residue model is used to identify the variation of the Thiele-Small parameters with temperature. Both the Metropolis–Hastings and the affine invariant ensemble sampling (AIES) algorithms are then employed to sample the posterior distribution of the Thiele-Small parameters, and their performances are compared. Metropolis–Hastings exhibited bias, underdispersion and convergence failure when estimating correlated parameters, whereas the ensemble sampler efficiently captured the full posterior at higher computational cost. Uncertainty propagation using the AIES-derived posteriors produced predictive intervals for the FRF and absorption coefficient that fully encompassed the experimental data.

1. Introduction

Managing noise remains a significant concern across multiple engineering domains, particularly in contexts such as environmental noise control and sound attenuation in open ducts. Classical approaches usually rely either on passive noise control solutions, such as sound-absorbing materials, resonators, or perforated honeycomb liners [1], or in active noise control (ANC) using phase inversion techniques such as the filtered-x least-mean-square (FxLMS) algorithm [2]. As an alternative approach, active impedance control has emerged as a promising technique [3]. This approach offers advantages over traditional passive methods by enabling adaptive behavior in response to varying operating conditions, while minimizing the problems related to secondary path estimation and stability related to ANC. Building upon this idea, Rivet et al. [4] developed a broadband electroacoustic absorber (EA) concept based on a feedforward control scheme. In this design, a loudspeaker is employed as an actuator to realize a desired acoustic impedance through feedback from collocated pressure measurements, substituting the classical shunting technique. This approach is based on

---

* Corresponding author.
E-mail address: leonardo.ferreira@femto-st.fr (L. Ferreira).

https://doi.org/10.1016/j.ymssp.2026.113970
Received 11 August 2025; Received in revised form 18 December 2025; Accepted 30 January 2026

a mechanical-model-inversion technique that avoids the complications related to the inversion of the electrical inductance in the impedance control. This control strategy has demonstrated great versatility and subsequent research has focused on assessing the performance and constraints of such devices [5–7].

The main drawback of the mechanical-model inversion technique is the need for a precise definition of the mechanical model of the loudspeaker [4]. Investigations by De Bono et al. [8] and Volery et al. [9] have considered the impact of different mechanical models and control strategies in the performance of EAs. These models are typically defined using the Thiele-Small parameters, which describe the interaction between electrical signals and mechanical loads, enabling the evaluation of performance aspects such as frequency response, efficiency, and sound quality. However, one of the principal sources of uncertainties on the Thiele-Small parameters is the temperature variation, and this has not yet been systematically explored under the context of EAs. This subject gains particular relevance in light of recent experiments involving EAs in ducts with significant airflow [10] or even turbofan engine representative rigs [11,12], where the thermal environment is highly variable under real operating conditions. Recent work also demonstrated that electroacoustic absorbers present viscoelastic properties highly dependent on the temperature [13], with direct impact on the control of the acoustic impedance and passivity of these devices.

Part of the temperature dependency observed in loudspeakers originates from the diverse materials used in their construction. The spider, a flexible component that centers the voice coil and provides a restoring force during diaphragm motion, is commonly made of impregnated textiles such as cotton, poly-cotton, or other composite materials. The surround may incorporate materials like rubber, foam, coated fabrics, or diaphragm materials [14]. Previous studies have investigated the temperature dependency of loudspeaker materials in the context of viscoelastic modeling [15], heat transfer characteristics [16], thermal variations in the coil [17], and nonlinear frequency behavior [18].

Beyond temperature effects, variations in manufacturing and assembly processes can also impact loudspeaker characteristics, as even with quality control, nominally identical drivers may exhibit significant variability in their Thiele-Small parameters [19]. Chojnacki [20] assessed the dispersion in Thiele-Small parameters across five different commercial loudspeaker models, using 10 samples for each, and demonstrated that while the nominal property variation was up to 10%, actual measurements revealed parameter variations as high as 20%. Bellini and Farina [21] conducted an empirical analysis of the influence of manufacturing deviations on loudspeaker parameters. They produced sample units with slight differences in physical properties, such as cone weight, membrane edge thickness, and membrane pulp quality, as well as in assembly details, including gluing of moving parts and connections between dome and cone. Their results indicated that variations in individual components had a greater impact on performance than those arising from assembly inconsistencies. Uncertainties in Thiele-Small parameters can directly impact the performance of electroacoustic absorbers both by adding error in the mechanical model, thereby introducing uncertainty in the resonance frequency, and by adding temperature-related bias on these parameters. Information about the uncertainty and variation of these parameters can increase their reliability in applications under dynamic thermal environments.

Although previous studies have investigated the temperature dependency of loudspeaker material properties and addressed uncertainties in the manufacturing of these devices, this work is the first to systematically characterize the temperature dependence of the Thiele-Small parameters in EAs over a broad range (−10 °C to +50 °C) and to quantify its impact on EA performance via uncertainty propagation. The effects of temperature on the mechanical parameters, mass (M_{ms}), resistance (R_{ms}), and stiffness (K_{mc}), are experimentally evaluated. Posterior distributions of the Thiele-Small parameters are then inferred within a Bayesian framework: both the Metropolis–Hastings MCMC algorithm and the affine-invariant ensemble sampler (AIES) [22] are employed. These two sampling methods are systematically compared in terms of convergence, mixing behavior, and computational efficiency, with particular attention to their ability to explore tightly correlated posterior distributions. Finally, the resulting posterior probability distribution functions (PDFs) are propagated through the pole-residue model to predict frequency response functions (FRFs) and the normal absorption coefficient, which are validated against measurements.

Towards this background, Section 2 provides a theoretical contextualization of EAs, detailing the mechanical model adopted for the loudspeaker and the methodology for parameter identification based on experimental measurements of acoustic impedance. Section 3 describes the theoretical basis of the Bayesian inference process for uncertainty quantification, and outlines the strategy for uncertainty propagation. Section 4 details the experimental setup used to measure the acoustic impedance under varying temperature conditions, following the ASTM E1050-24 standard [23]. Section 5 presents the results for the identification of the Thiele-Small parameters with respect to the temperature. Section 6 presents the Bayesian inference results, and Section 7 concludes with final remarks and suggestions for future research directions.

2. Dynamics of electroacoustic absorbers

The underlying theoretical foundations behind the dynamics of EAs, the pressure-based control strategy, and the methodology for identifying the Thiele-Small parameters are presented in this section.

2.1. Single-degree-of-freedom loudspeaker model

Fig. 1a shows an EA constructed using a loudspeaker and four microphones. It operates based on a pressure-current control scheme, as illustrated in Fig. 1b. This configuration considers an oscillator driven by a coil placed within a permanent magnetic field [24]. Based on the pressure measured in front of the diaphragm, a digital controller adjusts the current supplied to the coil to regulate the system's acoustic impedance. The mechanical behavior of the device can be modeled as single-degree-of-freedom (1DOF) system, as depicted in the free-body diagram in Fig. 1c. For modeling the mechanical dynamics of the system, the hypothesis of a

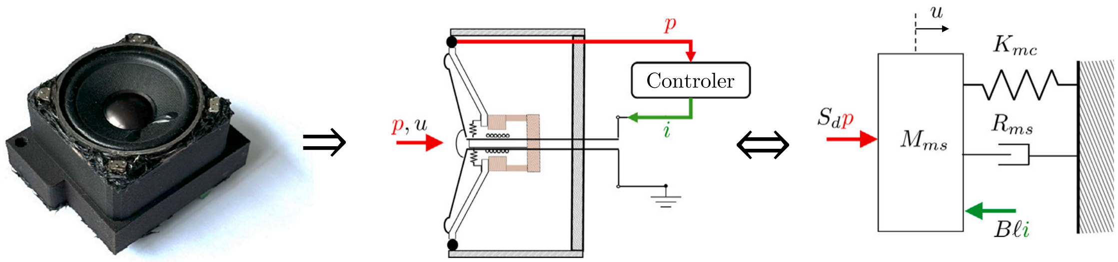

(a) (b) (c)

Fig. 1. EA considered in this study: (a) Photograph of the device, composed of a loudspeaker mounted over a closed box with four microphones, (b) Schematic representation of the pressure-current control, and (c) equivalent diagram of the system. In the diagrams, red indicates the measured quantities, specifically the pressure, while green denotes the controlled parameters.

linear system with small forces imposed by the pressure wavefield and small displacements is assumed. Therefore, the equilibrium of forces yields:

$$M_{ms}\frac{dv(t)}{dt} = S_d p(t) - B\ell i(t) - R_{ms}v(t) - \left(\frac{1}{C_{ms}} + \frac{\rho c^2 S_d^2}{V_b}\right)\int v(t)dt, \tag{1}$$

where $v = \frac{du}{dt}$ is the diaphragm velocity, p is the surface pressure at the diaphragm, i is the electrical current flowing through the voice-coil, ρ is the air mass density, c is the speed of sound, V_b is the loudspeaker rear cabinet volume. The Thiele-Small parameters are represented by the mass of the driver diaphragm and coil assembly M_{ms}, the mechanical viscous resistance R_{ms}, the mechanical compliance of the surrounding suspension and the spider C_{ms}, the equivalent area of the driven diaphragm S_d, and the force factor of the moving coil Bl. Considering small displacements, the total mechanical stiffness can be represented as $K_{mc} = 1/C_{mc} = 1/C_{ms} + \rho c^2 S_d^2/V_b$, with C_{mc} the total mechanical compliance of the EA.

Considering the Laplace variable s and applying the Laplace transform to Eq. (1):

$$Z_m(s)V(s) = S_d P(s) - B\ell I(s), \tag{2}$$

where the capital letters indicate the quantities P, V, and I in the Laplace's domain, and Z_m represents the mechanical impedance of the closed-box loudspeaker

$$Z_m(s) = M_{ms}s + R_{ms} + \frac{K_{mc}}{s}, \tag{3}$$

The dynamic response of the diaphragm to an external acoustic disturbance can be described by its acoustic impedance, which is defined as the complex ratio of the total sound pressure $P(s)$ at the diaphragm to the diaphragm velocity $V(s)$. In the condition of open-circuit loudspeaker, i.e., the case where no current circulates through the coil, Eq. (2) yields

$$Z_{a0}(s) = \frac{P(s)}{V(s)} = \frac{Z_m(s)}{S_d}, \tag{4}$$

where Z_{a0} represents the acoustical impedance of the loudspeaker without the action of the controller.

2.2. Control strategies for pressure-based electroacoustic absorbers

The behavior of EAs can be controlled through $I(s)$ in Eq. (2) to adjust the acoustic impedance to a target value. An extensive discussion on acoustic impedance control techniques is presented by Malléjac et al. [25]. Considering a pressure-based local impedance control strategy [4,26], the transfer function between the pressure measurements and the imposed current to the loudspeaker coil can be written as

$$H(s) = \frac{I(s)}{P(s)}, \tag{5}$$

where $H(s)$ is the control transfer function. To impose a target acoustic impedance, Z_{at}, one can obtain the control law by substituting $I(s)$ from Eq. (5) into Eq. (2) and isolating $H(s)$

$$H(s) = \frac{1}{B\ell}\left(S_d - Z_m(s)\frac{V(s)}{P(s)}\right). \tag{6}$$

Factoring out S_d, substituting Z_m/S_d by Z_{a0}, and defining $P(s)/V(s)$ as a target impedance

$$H(s) = \frac{I(s)}{P(s)} = \frac{S_d}{B\ell}\left(1 - \frac{Z_{a0}(s)}{Z_{at}(s)}\right), \tag{7}$$

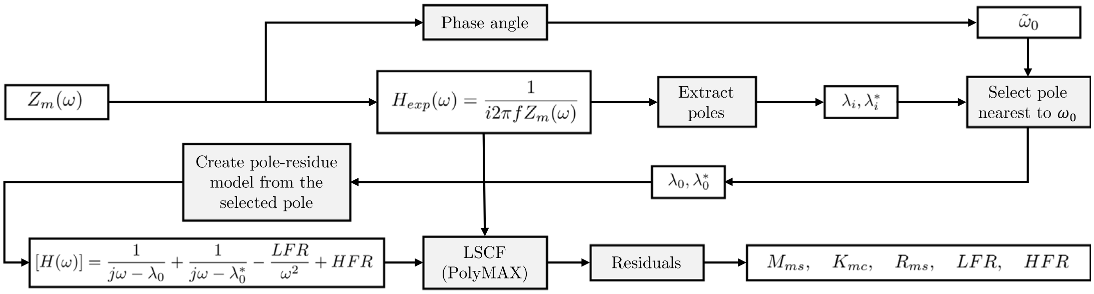

Fig. 2. Thiele-Small parameters identification procedure. LSCF stands for Least-Squares Complex Frequency-domain, LFR for low frequency residues, and HFR for high frequency residues.

where Z_{at} is the target impedance. Assuming a target impedance similar to that of a 1DOF system, it can be written as

$$Z_{at}(s) = \frac{P(s)}{V(s)} = \mu_1 \frac{M_{ms}}{S_d} s + R_{at}\rho_0 c_0 + \mu_2 \frac{K_{mc}}{sS_d}, \tag{8}$$

where μ_1 and μ_2 are two tunable coefficients that allow for controlling the effective mass and stiffness of the loudspeaker, respectively; R_{at} controls the target impedance to be achieved by the loudspeaker at the resonance, usually expressed as a fraction of the characteristic impedance of the air; ρ_0 is the air mass density, whereas c_0 is the speed of sound. As per Eqs. (7) and (8), both the control law and the target impedance are expressed in terms of the Thiele-Small parameters. These parameters are function of the material properties of the loudspeaker components, which are, in turn, sensitive to environmental conditions. Therefore, variations on the operational conditions could directly affect the behavior of the EA.

2.3. Thiele-small parameters identification

Fig. 2 illustrates the Thiele-Small parameter identification procedure based on experimental measurements of the acoustic impedance. The mechanical impedance obtained from Eq. (4) is used to derive the experimental frequency response function ($H_{exp}(\omega)$) in terms of displacement per force. The estimation of the natural frequency of the absorber ($\tilde{\omega}_0$) is obtained from the phase angle of the mechanical impedance, specifically at the frequency where the impedance's imaginary part is zero. Next, the nearest pole λ_i to $\tilde{\omega}_0$ in $H_{exp}(\omega)$ is used to build a pole-residue model $H(\omega)$. Then, the polyreference least-squares complex frequency-domain method (PolyMAX) [27] is used to fit $H(\omega)$ to $H_{exp}(\omega)$ and the model parameters in the form of the Thiele-Small parameters, M_{ms}, R_{ms}, and K_{mc}, and the low frequency (LFR) and high frequency (HFR) residues are obtained.

3. Proposed framework for uncertainty quantification

Fig. 3 presents the proposed framework for evaluating the dependence of the Thiele-Small parameters on the temperature, and the procedure of uncertainty quantification and propagation used in this work, based on five steps:

1. First, an experimental campaign is performed to evaluate the acoustic impedance of three different EAs under varying temperatures between −10 °C and +50 °C inside a thermal chamber using the procedures from the ASTM E1050-24. This is done through pressure measurements and the transfer function method using an impedance tube.
2. The resulting frequency response functions are used to identify the Thiele-Small parameters through the PolyMAX method.
3. Next, the identified Thiele-Small parameters are used in a Bayesian inference process to quantify the uncertainty. Two samplers are evaluated against each other in terms of convergence, sampling efficiency and computational cost: the Metropolis-Hastings sampler and the AIES
4. After selecting the optimal sampler, uncertainty quantification through Bayesian inference is performed across all EAs and temperatures with the AIES to obtain posterior PDFs for the parameters M_{ms}, R_{ms} and K_{mc}.
5. Finally, the uncertainty on the Thiele-Small parameters is propagated to the FRF and absorption coefficient of the EAs, defining confidence intervals (CIs) with respect to frequency and temperature.

This methodology has proven effective in other domains [28–30], and the remainder of this section presents the theoretical foundations of the Bayesian inference techniques employed in this work.

3.1. Uncertainty quantification through Bayesian inference

Physical systems exhibit inherent variations, such as differences in geometry, environmental conditions, and material properties. Consequently, even with an extensive dataset including numerous measurements of the acoustic impedance of the EA, uncertainty cannot be entirely eliminated. To include this variability in the parameters of the EA model, this study adopts the Bayesian paradigm

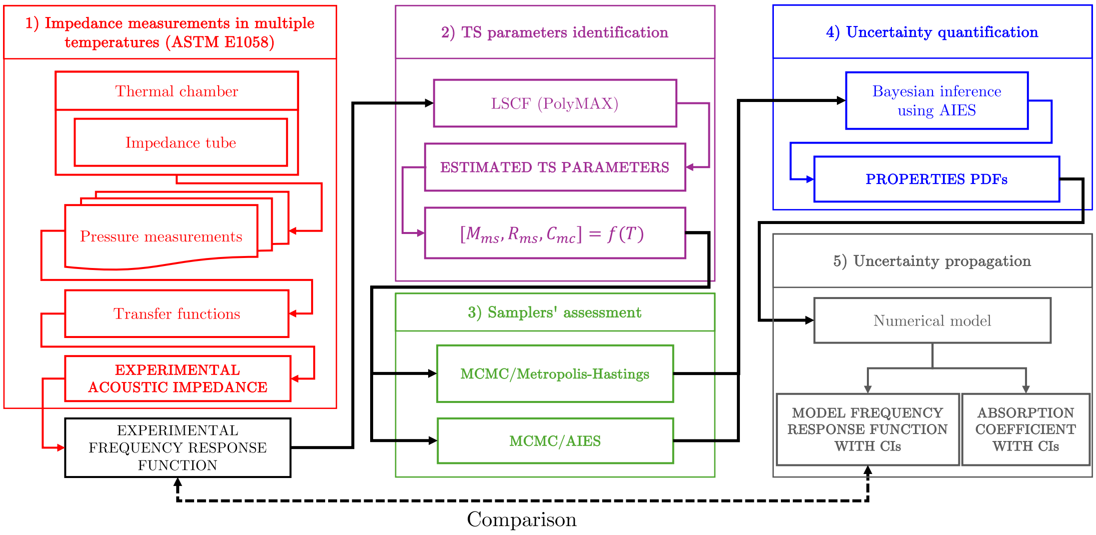

Fig. 3. Proposed framework for this work, divided in five steps. LSCF stands for Least-squares complex frequency-domain, MCMC for Markov-Chain Monte Carlo, AIES for affine-invariant ensemble sampler, PDF for probability density function, and CI for confidence interval.

as a statistical inference tool for dealing with parameters uncertainty [31]. For this, a probabilistic model with output $\mathbf{y}$ is defined by assuming an additive Gaussian error with zero mean and covariance matrix Σ to the model response $\mathcal{M}(\boldsymbol{\theta})$, that is:

$$\mathbf{y} = \mathcal{M}(\boldsymbol{\theta}) + \varepsilon \tag{9}$$

where ε is sampled from the multivariate normal distribution $\mathcal{N}(0, \Sigma)$. For the EAs, $\mathbf{y}$ can be represented by the FRFs of the system. If one have access to experimental data observations ($\mathcal{D}$) composed of N observations y_i, the analytical expression for the likelihood function $\pi(\mathcal{D}|\boldsymbol{\theta})$ is given by

$$\begin{aligned} \pi(\mathcal{D}|\boldsymbol{\theta}) &= \prod_{i=1}^{N} \mathcal{N}\left(y_i \mid \mathcal{M}(\boldsymbol{\theta}), \Sigma\right) \\ &= \prod_{i=1}^{N} \frac{1}{\sqrt{(2\pi)^{N_o} \det \Sigma}} \exp\left(-\frac{1}{2}\left(y_i - \mathcal{M}(\boldsymbol{\theta})\right)^{\mathrm{T}} \Sigma^{-1} \left(y_i - \mathcal{M}(\boldsymbol{\theta})\right)\right), \end{aligned} \tag{10}$$

with $(\bullet)^{\mathrm{T}}$ meaning transpose operation and Σ the covariance matrix of the N_o outputs of the model. Considering independence among samples, $\Sigma = \sigma_n^2 I$, with I being the identity matrix.

For applying the Bayesian inference framework, two assumptions are introduced: (i) as the model parameters, here represented as the Thiele-Small parameters, are random variables, a prior distribution $\pi(\boldsymbol{\theta})$ for the set of input variables $\boldsymbol{\theta}$ is proposed based on the prior knowledge about the system; (ii) Bayes' theorem is employed to update $\boldsymbol{\theta}$, gathering information from random data observations ($\mathcal{D}$). The posterior distribution $\pi(\boldsymbol{\theta}|\mathcal{D})$ is given by:

$$\pi(\boldsymbol{\theta}|\mathcal{D}) = \frac{\pi(\mathcal{D}|\boldsymbol{\theta})\pi(\boldsymbol{\theta})}{\pi(\mathcal{D})}, \tag{11}$$

where the denominator $\pi(\mathcal{D})$ is the marginal likelihood, i.e. it is a normalization constant that guarantees the definition of a probability density function with integral equal to unity. By considering a uniform prior distribution, Eq. (11) is simplified to $\pi(\boldsymbol{\theta}|\mathcal{D}) \propto \pi(\mathcal{D}|\boldsymbol{\theta})$ and the updated posterior PDF becomes proportional to the likelihood distribution. A log-likelihood version of Eq. (10) is implemented to avoid numerical problems related to the exponential calculation and substitute the product by a summation in the calculations:

$$\log(\pi(\mathcal{D}|\boldsymbol{\theta})) = -\sum_{i=1}^{N} \left(\frac{\log(2\pi\sigma_n^2)}{2} + \frac{1}{2\sigma_n^2} \left(\left|y_i - \mathcal{M}(\boldsymbol{\theta})\right|\right)^{\mathrm{T}} \left(\left|y_i - \mathcal{M}(\boldsymbol{\theta})\right|\right) \right). \tag{12}$$

Numerical samplers are commonly employed to approximate the posterior distribution by generating samples directly from it, without the need to analytically compute the likelihood function [32]. Several samplers are available in the literature [33,34], including classical Monte Carlo methods, e.g., Metropolis–Hastings [35] and Gibbs samplers [36], adaptive samplers such as the transitional Markov Chain Monte Carlo [37] and the AIES [22], and modern Monte Carlo samplers [38] including machine-learning based methods [39]. Two different samplers are proposed in this work: the Metropolis–Hastings and the AIES.

3.1.1. Metropolis–Hastings sampling

Algorithm 1 presents the implementation of the MCMC/Metropolis–Hastings sampling algorithm. The random variables $\boldsymbol{\theta}$ are constrained to the interval $[\boldsymbol{\theta}_{\min}, \boldsymbol{\theta}_{\max}]$, with the current state normalized as $\boldsymbol{\theta}' = (1 - \boldsymbol{x})\boldsymbol{\theta}_{\min} + \boldsymbol{x}\boldsymbol{\theta}_{\max}$; here, $\boldsymbol{x}$ is a random variable uniformly distributed in $[0, 1]$ representing candidates generated for the posterior distribution. These candidates are sampled from a normal distribution $q(\boldsymbol{\theta}^* | \boldsymbol{\theta})$ with a standard deviation of σ_p. Subsequently, the posterior distribution at the proposed sample are computed and the acceptance ratio is evaluated. Finally, the candidate is accepted or rejected based on the Metropolis–Hastings acceptance criteria.

Algorithm 1: MCMC/Metropolis–Hastings

```
Initialize $\boldsymbol{\theta}$ to $\boldsymbol{\theta}_0$;
for $i \leftarrow 1$ to $N$ do
    Propose $\boldsymbol{\theta}^*$ drawn from $q(\boldsymbol{\theta}^* | \boldsymbol{\theta})$;
    Calculate acceptance ratio $\alpha = \min\left(1, \frac{\pi(\boldsymbol{\theta}^* | \boldsymbol{D})}{\pi(\boldsymbol{\theta} | \boldsymbol{D})}\right)$;
    Draw $u$ uniformly from $(0, 1)$;
    if $u < \alpha$ then
        Accept the proposal: set $\boldsymbol{\theta} \leftarrow \boldsymbol{\theta}^*$;
    else
        Reject the proposal: keep $\boldsymbol{\theta}$ unchanged;
    end
    Save the current state $\boldsymbol{\theta}$ to the sample;
end
```

The hyperparameter σ_p controls the random walk step size to prevent the chain from becoming static while allowing for adequate exploration of the parameter space. Adjusting σ_p to achieve an acceptance rate of candidates between 15% and 50% ensures that the efficiency of the algorithm remains at least 80% [35].

3.1.2. Affine invariant ensemble sampler (AIES)

When evaluating the model from Eq. (3), both the mass and stiffness influence the imaginary part of the impedance. Moreover, these parameters are inversely proportional in the expression for the system's natural frequency, resulting in strong interdependence. Consequently, classical MCMC algorithms might struggle to efficiently sample from such correlated parameter spaces. To overcome this limitation, the AIES algorithm is proposed [22]. This algorithm is able to sample from highly skewed and correlated probability distributions by using affine transformations. The overall sampling strategy is described in Algorithm 2. The AIES operates an ensemble of L Markov chains in parallel, referred to as *walkers*. For a sample $x_i^{(t)}$ at the iteration t, each walker i updates its next position $x_i^{(t+1)}$ based on a randomly selected complementary walker $x_j^{(t)}$, with $i \neq j$. The candidate proposal is based on the difference between the current and complementary walkers, scaled by a stretch factor Z. The acceptance criterion is a modified version of the classical Metropolis–Hastings rule, adapted to account for the affine stretch transformation. A detailed analysis of this sampler, including its strengths, limitations, and comparisons with other sampling techniques, is provided by Allison and Dunkley [32].

3.2. Uncertainty propagation

After the inference of the posterior PDFs for the input parameters, their uncertainty can be propagated to the relevant quantities of the EAs' operation: the FRF and the normal absorption coefficient. The later is used as a performance metric for the EAs and it is defined as

$$\alpha(\omega) = 1 - |R(\omega)|^2, \tag{13}$$

where $\alpha(\omega)$ denotes the absorption coefficient and $R(\omega)$ is the reflection coefficient, given by

$$R(\omega) = \frac{Z_a(\omega)/\rho c - 1}{Z_a(\omega)/\rho c + 1}. \tag{14}$$

The normal absorption coefficient quantifies the proportion of incident acoustic energy absorbed by the EA. A value of 1 indicates total absorption, meaning the EA fully absorbs the incident wave with no reflection. Conversely, a value of 0 indicates total reflection, with no absorption of the incident energy, and a negative value corresponds to the loss of acoustical passivity (reflected energy higher than incident). An important threshold for α is the region $\alpha \geq \alpha_{th}$, where $\alpha_{th} = 1 - (\sqrt{2} - 1)^2$ corresponds to the case where the total sound intensity on the loudspeaker diaphragm is less than twice the sound intensity of the normal incident wave [40].

4. Experimental measurements of the acoustic impedance

The dataset for this study is collected from three nominally-identical EAs, each of them composed of a loudspeaker with 50 mm diameter, four microphones and an electronic board with a microcontroller that operates the device. The EAs are of the type presented in Fig. 1 and named cells A, B and C in the following. Differences between them can arise from the manufacturing

Algorithm 2: Affine invariant ensemble sampler

```
Initialize an ensemble of $L$ walkers $\{x_1^{(0)}, \dots, x_L^{(0)}\}$ in $\mathbb{R}^n$;
Set stretch-scale parameter $a > 1$;
for $t \leftarrow 0$ to $T - 1$ do
    for $i \leftarrow 1$ to $L$ do
        1. Select a "complementary" walker index $j \neq i$ uniformly from $\{1, \dots, L\} \setminus \{i\}$;
        2. Draw stretch factor
           $Z \sim g(z)\,, \quad g(z) \propto \begin{cases} \frac{1}{\sqrt{z}}, & z \in [1/a,\ a], \\ 0, & \text{otherwise}, \end{cases}$
           (so that $g\big(1/z\big) = z\, g(z)$);
        3. Propose
           $Y \;=\; X_i^{(t)} \;+\; Z\,\big(X_j^{(t)} - X_i^{(t)}\big).$
        4. Compute acceptance probability
           $\alpha = \min\Big(1,\ Z^{\,n-1}\, \dfrac{\pi\big(Y \mid D\big)}{\pi\big(X_j^{(t)} \mid D\big)}\Big).$
        5. Draw $u \sim \mathrm{Uniform}(0,1)$:
           $X_i^{(t+1)} = \begin{cases} Y, & u < \alpha, \\ X_i^{(t)}, & \text{otherwise.} \end{cases}$
    end
end
```

process of the components, and the assembly of the EA, which is manual. Their acoustic impedance is evaluated using the method proposed by the ASTM E1050-24 through an impedance tube built in aluminum, with a square cross-section of 50 mm and a length of 300 mm. Three PCB Piezotronics 130F21 microphones are positioned at distances of 50 mm, 100 mm, and 150 mm from the excitation source, and referenced as P_1, P_2, and P_3 in the following, respectively.

Data acquisition is performed using the NI cDAQ-9174 system, with NI 9234 module for data acquisition and NI 9263 module for signal generation. A Stage Line STA-102 amplifier is placed between the signal generator and the input speaker to amplify the input signal. The excitation consists of white noise signal in a frequency range between 300 Hz and 3000 Hz. The frequency limits are defined based on ASTM E1050-24, considering both limitations imposed by the microphone spacing and the cutoff frequency of the tube, which is approximately 3400 Hz.

Impedance measurements are conducted across a wide range of temperatures to evaluate the temperature dependency of the mechanical properties. A Climats PCH60 thermal chamber is used to control the temperature of the square impedance tube, covering a range from −10 °C to +50 °C. The impedance tube is mounted at the top of the chamber and subjected to a temperature cycle, as detailed in Fig. 4. The cycle begins with an initial pre-heating phase lasting 90 min, during which the temperature is raised to +55 °C. Following pre-heating, the temperature is held constant at +55 °C for 5 min to ensure system stabilization. Then, a constant cooling gradient of −0.5 °C/min is applied until the temperature reaches −15 °C, followed by a 5-minutes stabilization period. The temperature inside the impedance tube is monitored using a thermocouple, and data recorded at temperatures above +50 °C and below −10 °C are discarded. Three sequential pressure measurements are performed per minute, each during 10 s, and the system waits 30 s to start a new round. This cycle is repeated during all the temperature gradient duration, which results in 360 pressure measurements from +50 °C to −10 °C.

The sampling frequency is 51200 Hz and the post-processing of each 10 s measurement is made as follow: first, the measurements are divided into 10 blocks of 1 s, then, a power spectral density computation is made using the Welch's estimator through a Hanning window with 8192 points and a 50% overlapping for each block. The transfer function between microphones is then evaluated and averaged in the frequency domain for all blocks. Then, the acoustic impedance is determined in accordance with ASTM E1050-24 using the microphone pairs $P_1 - P_2$, $P_2 - P_3$, and $P_1 - P_3$. For each temperature, mass density and sound velocity of the air inside the tube are adjusted for each sample using the formulation proposed in the ASTM E1050-24 and the thermocouple readings. Fig. 5a-c illustrates the acoustic impedance near resonance and the corresponding FRFs for cells A, B, and C, with continuous temperature increment from −10 °C to +50 °C.

The three loudspeakers exhibit similar temperature-dependent behaviors, with the real part of the impedance reaching a minimum value around resonance, and the imaginary part being negative before resonance and positive after it. The real part of the impedance remains stable with respect to temperature below the characteristic impedance of air (represented by the dashed

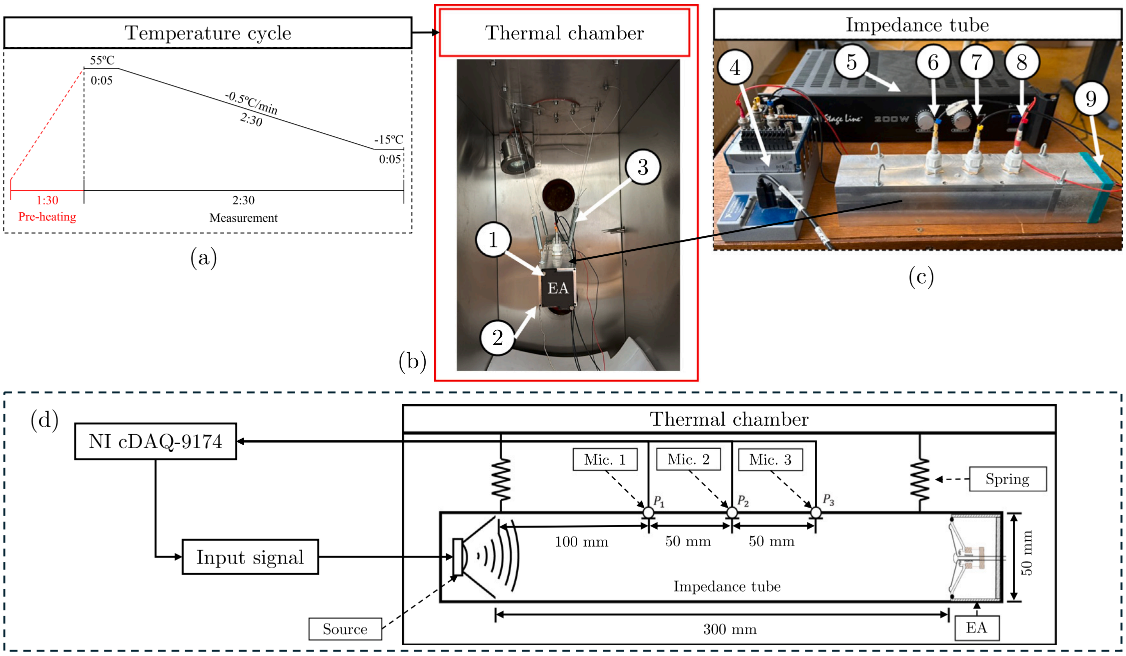

Fig. 4. Experimental setup for evaluating the acoustic impedance under varying temperature with: (a) temperature cycle used in the tests, with the time expressed using the format *hh:mm*, (b) Climats PCH60 thermal chamber with the impedance tube inside, (c) detail on the impedance tube and data acquisition system, and (d) schematic description of the experiment. In the figures, the numbers represent (1) the electroacoustic absorber, (2) the thermocouple, (3) the springs used to suspend the tube, (4) the NI cDAQ-9174, (5) the Stage Line STA-102 amplifier, and (6) the PCB 130F21 microphones P_1, (7) the PCB 130F21 microphones P_2, (8) the PCB 130F21 microphones P_3, and (9) the PCB input loudspeaker.

Table 1
Natural frequencies for EAs A, B and C.

	Cell A		Cell B		Cell C	
Temperature [C]	Natural frequency [Hz]	Variation [%]	Natural frequency [Hz]	Variation [%]	Natural frequency [Hz]	Variation [%]
−10	856.2	32.2	818.8	31.4	766.7	27.3
0	762.5	17.7	722.9	16.1	685.4	13.8
10	689.6	6.4	658.3	5.7	629.2	4.5
20	647.9	–	622.9	–	602.1	–
30	616.7	−4.8	608.3	−2.3	589.6	−2.1
40	602.1	−7.1	597.9	−4.0	579.2	−3.8
50	591.7	−8.7	591.5	−5.0	572.9	−4.8

black line) near resonance. Below resonance, the impedance increases, with this behavior becoming more pronounced in the samples collected below 10 °C, when it sharply rises. Additionally, there is a larger shift in the resonance frequencies of the loudspeaker at lower temperatures, which can be observed in the FRFs from the Figs. 5(d) to 5(f).

Fig. 6 presents the experimental dispersion of the natural frequency of the loudspeakers of the EAs A, B, and C estimated from the poles of the pole-residue model, while Table 1 summarize the corresponding results. Given the continuous variation of the temperature during the experiments, for each discrete temperature listed in Table 2, a set of experimental data with M realizations, bounded between ±0.5 °C of the selected temperature, is used to compute the reported average value. At 20 °C, the loudspeakers A, B, and C present natural frequencies of 647.9 Hz, 622.9 Hz, and 602.1 Hz, respectively. Between 20 °C and 50 °C, the natural frequency of the system varies to 591.7 Hz for loudspeaker A, 591.5 Hz for loudspeaker B, and 572.9 for loudspeaker C, which represents variations of −8.7%, −5.0%, and −4.8% variation, respectively. In the range from 20 °C to −10 °C, the natural frequency shifts to 856.2 Hz, 818.8 Hz, and 766.7 Hz for loudspeakers A, B, and C, representing variations of 32.2%, 31.4% and 27.3%, respectively. This behavior indicates nonlinear changes in the material properties as a function of temperature typical of viscoelastic materials.

5. Temperature influence on Thiele-Small parameters

The method described in Section 2.3 is applied to identify the Thiele-Small parameters of the EAs. Fig. 5d–f show the FRFs obtained using the mechanical impedance. The parameters are identified at discrete temperature levels ranging from −10 °C to

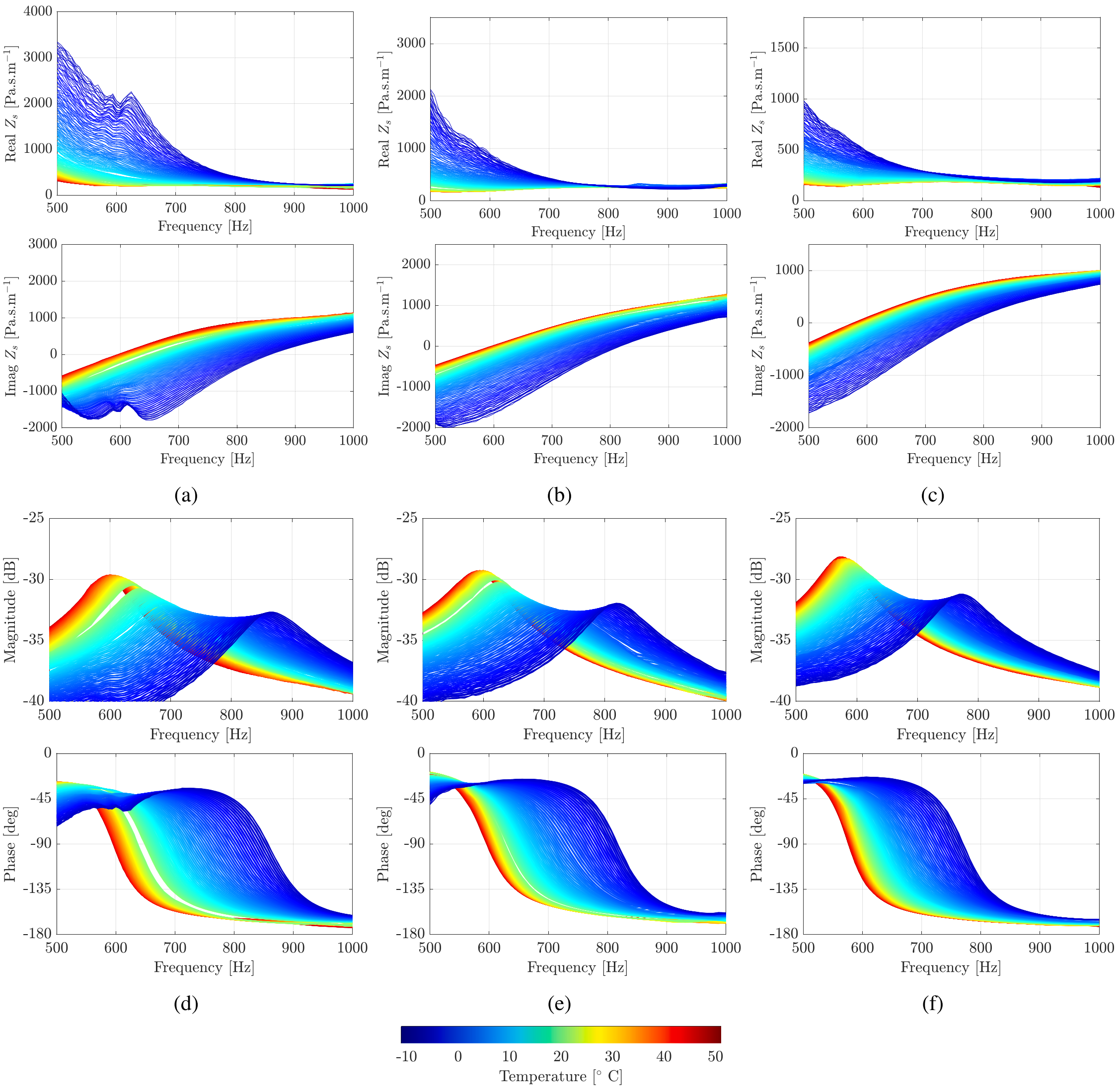

(a)
(b)
(c)
(d)
(e)
(f)

Fig. 5. Experimental results obtained from the impedance tube with varying temperature from −10 °C to 50 °C: real and imaginary measurements for the acoustic impedance from for (a) cell A, (b) cell B, and (c) cell C; and magnitude and phase of the FRF calculated from the mechanical impedance for (d) cell A, (e) cell B, and (f) cell C. The colors for all the charts represent the temperature of the sample, in accordance withe the temperature scale displayed at the figure. The reference for the magnitude of the FRFs in dB scale is 1 m N^{-1}.

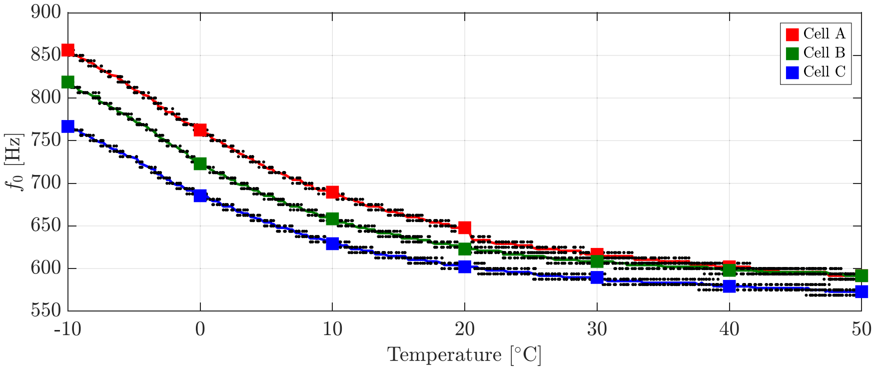

Fig. 6. Variation of the natural frequency of the EAs A, B and C with respect to the temperature. Each black dot represents an experimental realization, full lines indicate the average value, and the squares indicate the average value at temperatures of −10, 0, 10, 20, 30, 40, and 50 °C.

Table 2

Mechanical Thiele-Small parameters identified for temperature range from −10 °C to 50 °C for cells A, B, and C. For this study, the values measured at 20 °C are considered as reference.

Cell	Parameter	Temperature [°C]							Mean	STD.	CV [%]
		−10	0	10	20	30	40	50			
A	M_{ms} [g]	0.525	0.545	0.542	0.551	0.586	0.589	0.592	0.562	0.027	4.8
	R_{ms} [Ns/m]	0.324	0.402	0.355	0.298	0.266	0.266	0.274	0.312	0.052	16.5
	K_{mc} [kN/m]	15.2	12.6	10.1	9.1	8.7	8.4	8.2	10.3	2.64	25.6
B	M_{ms} [g]	0.508	0.488	0.502	0.507	0.504	0.498	0.498	0.501	0.007	1.3
	R_{ms} [Ns/m]	0.287	0.370	0.323	0.259	0.240	0.239	0.251	0.281	0.049	17.5
	K_{mc} [kN/m]	13.3	10.1	8.5	7.6	7.2	6.9	6.7	8.6	2.36	27.4
C	M_{ms} [g]	0.470	0.459	0.474	0.480	0.493	0.498	0.498	0.482	0.015	3.1
	R_{ms} [Ns/m]	0.255	0.324	0.278	0.225	0.203	0.198	0.203	0.241	0.047	19.7
	K_{mc} [kN/m]	10.9	8.5	7.3	6.8	6.6	6.5	6.3	7.6	1.65	21.8

50 °C, in increments of 10 °C. Due to the continuous temperature variation within the thermal chamber and the accuracy of the thermocouple, samples corresponding to each target temperature are selected within a ±0.5 °C margin.

As the assumption of a 1DOF system is valid only near resonance, a −3.0 dB criterion from the resonance peak is applied to isolate the valid region of the FRF and apply the identification algorithm described in Fig. 2. Fig. 7 and Table 2 present the estimated Thiele-Small parameters with respect to temperature for the cells A, B, and C. In Fig. 7, the multiple data points at the same temperature result from two factors: experimental samples within the ±0.5 °C margin and different microphone pair permutations on the impedance tube (i.e., parameters estimated from pressure pairs $P_1 - P_2$, $P_2 - P_3$, and $P_1 - P_3$). The mass of the three loudspeakers remains approximately constant, with small experimental variations indicated by the coefficient of variation (CV), likely due to measurement noise. In contrast, the resistance and stiffness exhibit considerable variation with temperature, showing nonlinear behavior. Resistance increases from −10 °C and reaches a maximum near 0 °C, after which it decreases and stabilizes around 30 °C. The stiffness decreases with temperature with a greater rate of change between −10 °C and 20 °C when compared to the region between 20 °C to 50 °C. This nonlinearity in stiffness over temperature corresponds to the behavior observed in the resonance frequency both above and below 20 °C.

Figs. 7(d) and 7(e) present the LFR and HFR parameters of the pole-residue model as a function of temperature. These parameters exhibit an approximately constant average with respect to temperature variation. Notably, the imaginary parts of LFR and HFR are concentrated around zero, as observed in the distributions shown on the right side of the lower charts in Figs. 7(d) and 7(e). These distributions have a narrow peak around zero, in contrast to what is observed for the real part of the residues. The observed dispersion, for instance at 30 and 40 °C, is likely related to experimental noise, as these parameters are derived from the residues computed during the identification process.

Near resonance, the loudspeaker dynamics is dominated by the of the single-degree-of-freedom system characterized by its natural frequency ω_n and damping ratio ζ. In this region, the Thiele-Small parameters M_{ms}, R_{ms}, and K_{mc} dominate the response of the system, while HFR and LFR act mainly as baseline offsets that do not alter the local peak shape or level. Because the inference objective is to characterize behavior in this resonance window, the Bayesian inference is therefore restricted to M_{ms}, R_{ms} and K_{mc}; the residue terms are fixed to their temperature-dependent sample means.

6. Uncertainty quantification and propagation

The Bayesian framework is used to update the Thiele-Small parameters of cells A, B and C and to propagate the resulting uncertainty to the FRF and the normal-incidence absorption coefficient. Despite being nominally identical, the identification of the Thiele-Small parameters in Section 5 showed that the properties vary among individual cells. Therefore, each cell is treated as a separate dataset, and the inference process is repeated for each one of them. The complete workflow is described for cell A and then replicated for cells B and C.

Under this framework, prior distributions for M_{ms}, R_{ms} and K_{mc} are defined from the identification results in Section 5. Posterior distributions are obtained via MCMC sampling, accounting for epistemic uncertainty. Sampling is performed with both the Metropolis–Hastings algorithm and the AIES. The resulting parameter uncertainty is propagated through the pole-residue model to yield posterior predictive distributions for the FRF and the absorption coefficient, which are then compared to experimental measurements.

6.1. Prior information of the Bayesian inference process

For each cell and at each temperature from −10 °C to 50 °C in 10 °C increments, a prior distribution $\pi(\theta)$ is specified. Uniform priors are centered on the mean Thiele-Small parameters in Table 2, with bounds of ±20% to ensure adequate exploration by the samplers. Table 3 gives the bounds for cell A as an example.

Given the prior $\pi(\theta)$ and a reference temperature, a dataset of M experimental realizations lying within ±0.5 °C of the target temperature is assembled. Posterior sampling was performed using both the Metropolis–Hastings MCMC algorithm (Algorithm 1) and the AIES algorithm (Algorithm 2).

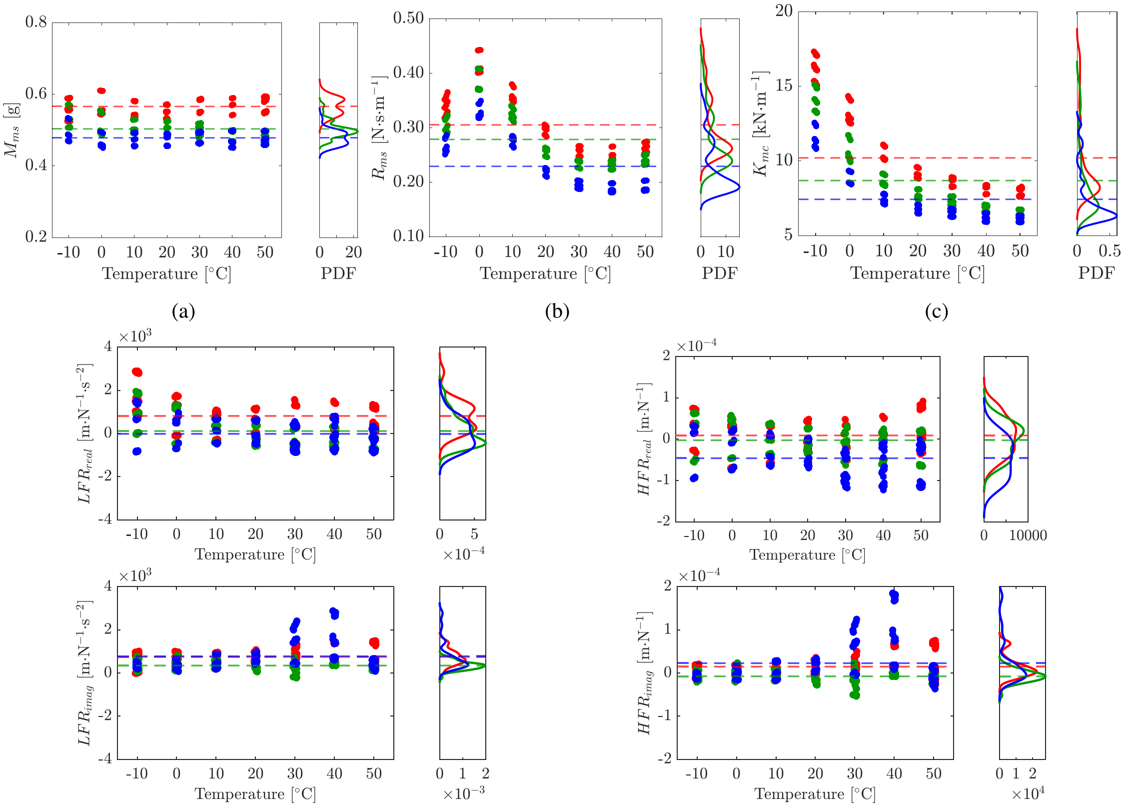

(a) (b) (c)

(d) (e)

Fig. 7. Thiele-Small parameters with respect to temperature for cells A, B, and C: (a) M_{ms}, (b) R_{ms}, (c) K_{mc}; and residues from the pole-residue model: (d) real and imaginary parts of the low frequency residues, and (e) real and imaginary part of the high frequency residues. In all charts, (•) represent data for cell A, (•) for cell B, (•) for cell C, and the dashed lines indicate the average value for each cell. LFR stands for low frequency residue and HFR for high frequency residue.The multiple data points at the same temperature result from the experimental samples within the ±0.5 °C margin and different microphone pair permutations on the impedance tube (i.e., parameters estimated from pressure pairs $P_1 - P_2$, $P_2 - P_3$, and $P_1 - P_3$).

Table 3
Prior distributions of model input parameters and model discrepancy hyper-parameter.

		Model parameters		
Parameter		M_{ms}	R_{ms}	K_{mc}
Unit		[g]	[Ns/m]	[kN/m]
Distribution		Uniform	Uniform	Uniform
Temperature [°C]	−10	(0.420, 0.630)	(0.259, 0.389)	(12.2, 18.2)
	0	(0.436, 0.654)	(0.322, 0.482)	(10.1, 15.1)
	10	(0.434, 0.650)	(0.284, 0.426)	(8.1, 12.1)
	20	(0.441, 0.661)	(0.238, 0.358)	(7.3, 10.9)
	30	(0.469, 0.703)	(0.213, 0.319)	(7.0, 10.4)
	40	(0.471, 0.707)	(0.213, 0.319)	(6.7, 10.1)
	50	(0.474, 0.710)	(0.219, 0.329)	(6.6, 9.8)

6.2. Metropolis–Hastings and AIES assessment

For the Metropolis–Hastings, single chains are created by drawing random samples within the prior bounds. At each iteration, a candidate θ^* is proposed, the log-likelihood from Eq. (12) is evaluated over the M measurements, and the Metropolis criterion determines acceptance. Proposal variance and the model-discrepancy variance are tuned to maintain a 20 to 50% acceptance rate [35].

For the AIES, an ensemble of $L = 10$ walkers ($L \geq 2D$, where D is the number of parameters) is initialized within the prior bounds. Each iteration applies a stretch-move proposal (Algorithm 2), computes the FRF via the pole-residue model, evaluates the

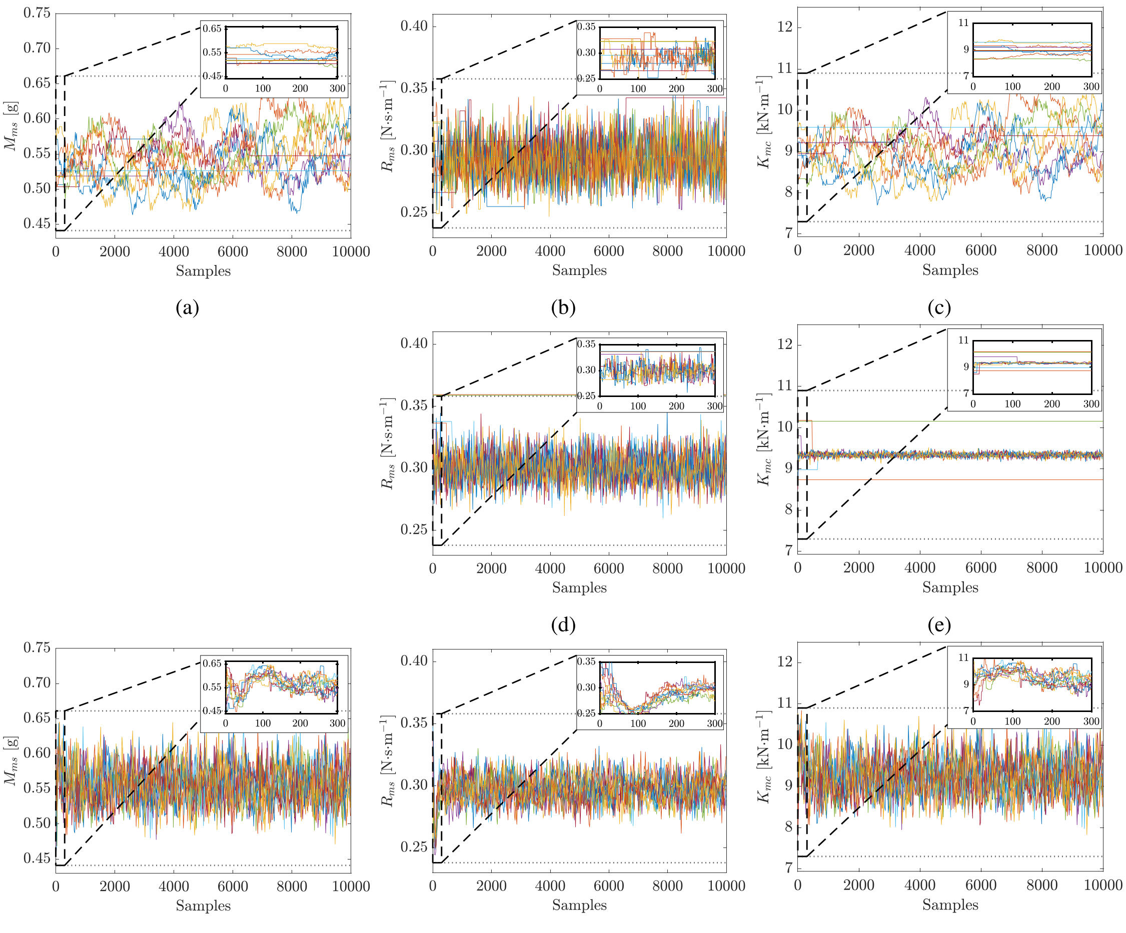

(a) (b) (c)

(d) (e)

(f) (g) (h)

Fig. 8. Random walk comparison for the inference process sampling 10 Markov chains for the Thiele-Small parameters of cell A at 20 °C: (a) M_{ms}, (b) R_{ms}, and (c) K_{mc} using the Metropolis–Hastings sampling algorithm and considering the three Thiele-Small parameters simultaneously; (d) R_{ms}, and (e) K_{mc} using the Metropolis–Hastings sampling algorithm and considering only two Thiele-Small parameters; and (f) M_{ms}, (g) R_{ms}, and (h) K_{mc} using the AIES and considering the three Thiele-Small parameters simultaneously. The horizontal dotted lines indicate the inference walk limits and the small inserts in upper right corner detail the chain behavior in the first 300 samples.

log-likelihood, and accepts or rejects according to the modified Metropolis criterion. The stretch factor a is chosen to yield an acceptance rate near 50% [32]. Both samplers run for 10 000 samples per chain and convergence is assessed a *posteriori*.

Initial Metropolis–Hastings trials targeting M_{ms}, R_{ms} and K_{mc} simultaneously exhibited non-stationary behavior in M_{ms} and K_{mc}. As shown in Fig. 8(a) and 8(c), several chains exhibit monotonic drift rather than oscillating around a stationary mean. This is mostly due to a strong correlation between these parameters, arising from their inverse relation in the natural-frequency term of the pole-residue model. Since the Metropolis–Hastings proposal is isotropic in parameter space, it cannot efficiently navigate the nonlinear correlation arising from this coupling between M_{ms} and K_{mc}. Additionally, as the likelihood penalizes deviations in natural frequency, compensatory shifts between M_{ms} and K_{mc} produce large likelihood fluctuations, preventing convergence despite extensive tuning to achieve the target acceptance rate between 20% and 50%. The insets in Figs. 8(a)–8(c) corroborate this hypothesis, showing that the sampler behavior varies considerably between chains, with several chains presenting flat traces and failing to explore the prior efficiently.

Sampling was therefore restricted to R_{ms} and K_{mc} given the smaller CV observed M_{ms} (Table 2) and that this parameter is dominated by the membrane mass, which is, in principle, insensitive to temperature changes. Figs. 8(d) and 8(e) show ten independent Metropolis–Hastings chains initialized uniformly within the prior bounds. Compared to three-parameter sampling, the two-parameter chains exhibited improved convergence: most walkers for both R_{ms} and K_{mc} settled into the same posterior region. However, a subset of chains remained trapped at their initial values, as evidenced by the flat traces in Fig. 8(e). In these cases, the initial parameter combination produced an FRF that deviated substantially from the experimental data, and the local proposal mechanism failed to locate higher-likelihood regions. This behavior can be mitigated by narrowing the initialization range or by increasing the proposal variance $q(\boldsymbol{\theta}^*|\boldsymbol{\theta})$. The former requires dataset-specific selection of initial points, whereas the latter enhances

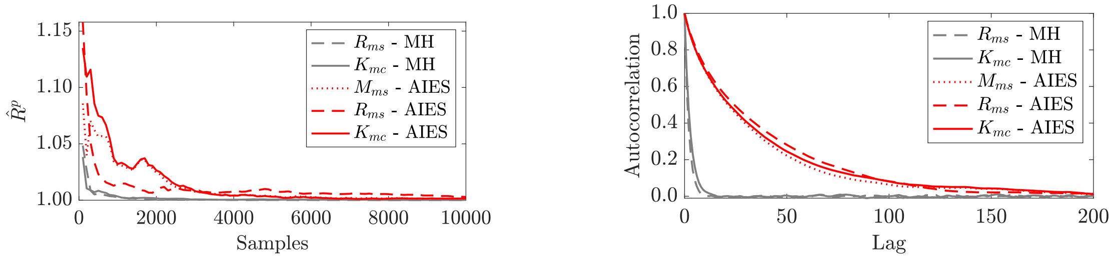

(a) (b)

Fig. 9. Convergence metrics for the Metropolis–Hasting and AIES sampling algorithms for the sampling at 20 °C: (a) Gelman–Rubin potential scale reduction factor for each parameter and (b) autocorrelation between samples. MH stands for Metropolis–Hastings and AIES for affine-invariant ensemble sampler.

Table 4
Metrics comparing the performance of Metropolis–Hastings and AIES. A_{cor} stands for autocorrelation between samples and ESS for effective sample size.

	Simulation time [s]	# of chains	Samples after burn-in	Total number of samples	A_{cor}	ESS	Cost per effective sample [ms]
MH	1.4	1	8000	8000	16	500	2.8
AIES	16.2	10	6000	60 000	200	300	54.0

global exploration at the cost of higher rejection rates near the posterior mode. In this study, the proposal variance was tuned to maintain a 20%–50% acceptance rate [35].

Given the inability of Metropolis–Hastings to converge when sampling all three Thiele-Small parameters concurrently and its sensitivity to initialization, the AIES was applied to sample the full correlated posterior. Figs. 8(f)–8(h) show the ensemble trajectories for M_{ms}, R_{ms} and K_{mc}. Insets in the upper-right panels demonstrate rapid mixing and stationarity across walkers, which explore the entire prior support and efficiently concentrate on the posterior. A stretch factor $a = 2$ achieved the target acceptance rate of approximately 50%, in agreement with [32].

Convergence and sampling robustness were assessed using the Gelman–Rubin potential scale reduction statistic $\hat{R}^p$ [41], which compares within-chain variance to between-chain variance across L independent Markov chains. Upon convergence, the second-moment estimate from each chain agrees with that of the pooled ensemble, driving $\hat{R}^p$ toward unity. Convergence was diagnosed by plotting $\hat{R}^p$ as a function of the number of samples. Fig. 9(a) shows $\hat{R}^p$ for both samplers. The Metropolis–Hastings chains fall below 1.05 within approximately 500 samples and approach unity by 1000 samples. In contrast, the AIES sampler requires roughly 2000 samples to reach 1.05 and about 4000 samples to approach unity, reflecting the additional cost of information exchange among walkers. Accordingly, a burn-in of 20% (2000 samples) was applied to Metropolis–Hastings, and 40% (4000 samples) to AIES (see Fig. 9).

Fig. 9(b) compares the sample autocorrelation (A_{cor}) time for R_{ms} and K_{mc} under Metropolis–Hastings and AIES. The Metropolis–Hastings chains decorrelate rapidly, with autocorrelations falling below 0.1 by lag ≈ 6 and effectively vanishing ($A_{\mathrm{cor}} < 0.01$) by lag ≈ 16. In contrast, AIES exhibits a slower decay: autocorrelations exceed 0.1 until lag ≈ 100 and only approach zero near lag ≈ 200, yielding a larger integrated autocorrelation time.

Table 4 summarizes wall-clock time, post-burn-in sample counts, autocorrelation times, effective sample sizes (ESS) and cost per effective sample for both algorithms. Metropolis–Hastings required only 1.4 s to generate 8000 post-burn-in samples with an integrated autocorrelation of 16 and ESS of 500, resulting in a cost of 2.8 ms per effective sample. AIES, with ten walkers, took 16.2 s to produce 60 000 post-burn-in samples (6000 per walker), but had an integrated autocorrelation of 200 and ESS of 300, yielding 54 ms per effective sample. Thus, although AIES provides robust exploration of the correlated posterior, its higher autocorrelation and computational overhead reduce sampling efficiency.

6.3. Parameter updating for a single-EA case

After assessing both algorithms, the inference was repeated for cell A at temperatures from −10 °C to 50 °C. Fig. 10 summarizes the posterior distributions. Figs. 10(a)–10(c) show the posteriors for M_{ms}, R_{ms} and K_{mc} at 20 °C, while Figs. 10(d)–10(f) plot the 95% CIs for each parameter across the full temperature range.

The Metropolis–Hastings sampler yielded biased posterior for R_{ms} at 0 °C (Fig. 10(e)) and consistently underestimated the variance of K_{mc}, as indicated by overly narrow CIs (Fig. 10(f)). In contrast, the AIES-derived intervals that reliably encompassed the experimental measurements at all temperatures. The shortcomings of the Metropolis–Hastings, together with its failure to sample

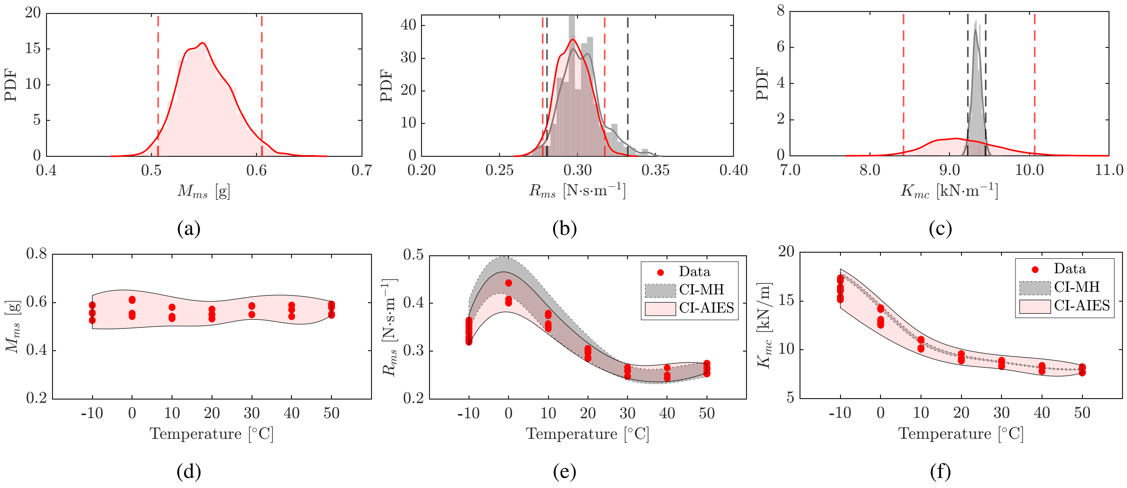

Fig. 10. Posterior distributions at 20 °C for (a) M_{ms}, (b) R_{ms}, and (c) K_{mc}. The vertical dashed lines indicate the 2.5% and 97.5% percentiles, and the gray and red indicates the Metropolis–Hastings and the AIES algorithms, respectively. Properties with respect to temperature with CIs from −10 °C to 50 °C sampled using Metropolis–Hastings and AIES algorithms for (d)M_{ms}, (e) R_{ms}, and (f) K_{mc}. The red dots indicate the experimental samples and the shaded areas represent the 95% CIs (obtained from the 2.5% and 97.5% percentiles). There is no distribution or CI for M_{ms} using the Metropolis–Hastings algorithm because it was not possible to sample M_{ms}, R_{ms}, and K_{mc} simultaneously. MH stands for Metropolis–Hastings, AIES for affine-invariant ensemble sampler, and CI for confidence intervals.

M_{ms} and its convergence difficulties, led to the selection of the AIES despite its higher computational cost. Consequently, all subsequent analyses present the AIES-derived posteriors exclusively.

Fig. 11 presents the resulting PDFs from the inference process using the AIES algorithm applied to cell A data, composed of the samples from all 10 walkers and processed using a 40% burn-in. The correlation between M_{ms} and K_{mc} manifested as aligned points in the lower left chart of Fig. 11(a). Similar to the results obtained in Table 2 and Fig. 7, M_{ms} presents an approximately constant value. In the inference process, this translates to concentrated unimodal posterior PDFs with temperature variation in Fig. 11. The inference process provides information on the dispersion of the properties, represented by the variance of the distribution (or the coefficient of variation, CV, presented in Table 5) and the percentiles.

For R_{ms}, the identified value for cell A at 20 °C is 0.298 Ns/m, as shown in Table 2, while the inference process yields a distribution with an $\mu_{R_{ms}}$ of 0.30 Ns/m. Therefore, both approaches produce nearly identical results that fall within the 95% CIs, delimited by the 2.5% and 97.5% percentiles of 0.27 and 0.33 Ns/m, respectively. Similar observations can be made for R_{ms} at the other temperatures presented in Table 5.

Evaluating K_{mc} for cell A at 20 °C, the identification process results in 9.1 kN/m, as reported in Section 5, while the inference process produces a distribution with an $\mu_{K_{mc}}$ of 9.03 kN/m. Both values differ by less than 1% and fall within the 95% CIs defined by the 2.5% and 97.5% percentiles of 8.87 and 9.17 kN/m, respectively. The same evaluation can be extended to the other temperatures in Table 5.

6.4. Uncertainty quantification through AIES - multiple cells

After the evaluation of the single cells, the same procedure is repeated for cells B and C. The AIES algorithm is used to sample the posterior distributions from priors limited as presented in Table 3, but adapted for cells B and C, i.e., the average values for each temperature from Table 2 perturbed within ±20% bounds. For each cell and each temperature, 10 walkers are used to sample 10 000 samples each, and a burn-in of 40% is used to retain only the stable part of the chains. Fig. 12 presents the results for the inference process.

The marginal posterior densities of M_{ms} for cells A, B and C (Fig. 12(a)) are all unimodal and roughly Gaussian in shape. When viewed as a function of temperature (Figs. 12(d) and 12(h)), the posterior means display only a mild, non-monotonic dependence on temperature, varying by less than 5% across the full −10 °C to 50 °C range. This variation is in line with the variations observed in the identification process of Section 5. The 95% CIs maintain a nearly constant width for each cell, indicating that the mass estimate is essentially temperature-independent. Moreover, the shape and overlap of the CIs for all three cells implies no statistically significant difference in M_{ms} beyond a constant offset in their posterior means.

Evaluating the posteriors for R_{ms} of cells A, B, and C in Fig. 12(b) reveals similar distribution shapes across the cells, although spanning different ranges. The most concentrated distributions correspond to 50 °C, with posterior means of 0.27, 0.25, and 0.20 Ns/m for cells A, B, and C, respectively. As temperature decreases, both the posterior mean and standard deviation increase,

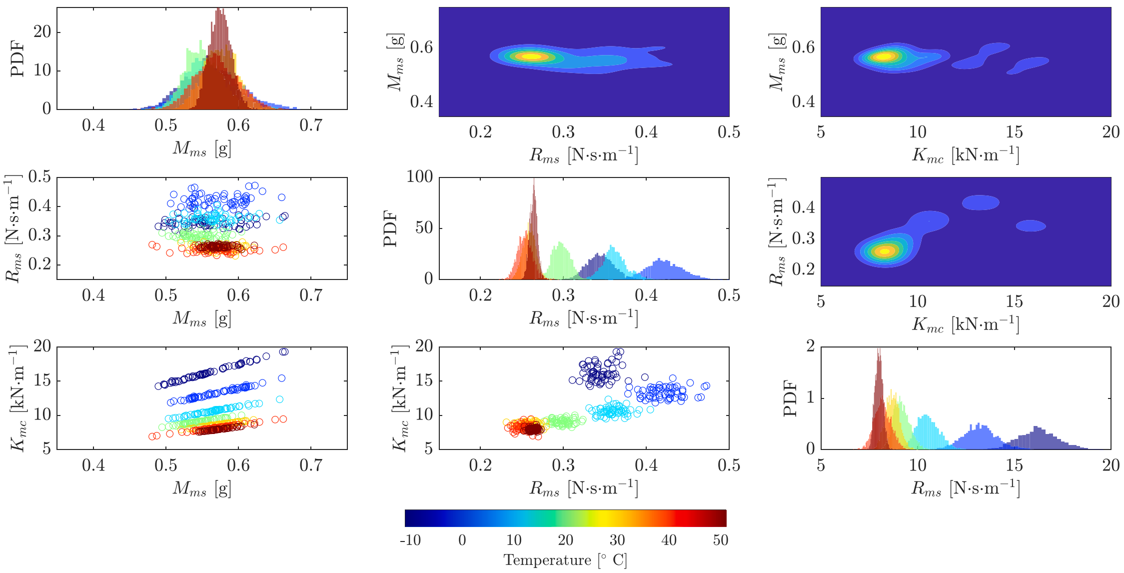

(a)

Fig. 11. Results for the Bayesian inference process for cell A using the AIES algorithm. Sampled distributions with respect to temperature presented using histograms, scatter and contour plots for the posterior distributions. The color bar indicate the temperature for the histograms and scatter plots from −10 °C to 50 °C, while the contour plots present the posterior distributions for all temperatures combined.

peaking at 0 °C. This trend suggests a viscoelastic behavior on the materials, with a glass transition at lower temperatures. Fig. 7 shows overlap in the identified values of R_{ms} for cells A and B at 0, 40, and 50 °C. In the inference results, this is further evidenced by the significant intersection of their CIs across all temperatures, as displayed in Fig. 12(b). Cell C, in contrast, overlaps with cell B only at temperatures of 0 °C and below, as reflected by the intersection of their CIs at these temperatures. Nevertheless, the CIs for all three cells exhibit similar shapes, indicating that while their posterior means differ, the underlying uncertainty distributions retain comparable characteristics.

Fig. 12(c) reveals that the posterior distributions of K_{mc} decrease monotonically with temperature, from roughly 18 kN/m at −10 °C down to about 6 kN/m at 50 °C, indicating a softening effect. Concurrently, the width of the 95% CI contracts over the same temperature range, indicating that stiffness is more tightly constrained at higher temperatures. Similar to the results for R_{ms}, all three cells posteriors exhibit similar shapes, indicating that the underlying uncertainty distributions retain comparable characteristics.

In all cases, the posterior CI capture both the systematic trends with temperature and the relative uncertainty in each parameter. While the means of M_{ms}, R_{ms}, and K_{mc} differ among the three cells, the overlapping CIs, in particular for M_{ms} and R_{ms}, suggest that inter-cell variability is modest compared to the temperature-induced shifts.

Table 5 presents a summary of the results obtained during the inference process. The average values obtained for each parameter and at each temperature closely correspond to the identified parameters in Table 2. However, the inference process provides additional information on the standard deviation (presented in Table 5 as the CV), as well as on the 95% CIs defined by the 2.5% and 97.5% percentiles. The results presented in Fig. 12 and in Table 5 indicate that the similarity in design among the devices extends to the properties of the assembled systems. This supports the feasibility of an identification process based on the Hierarchical Bayesian framework, similar to that proposed by Dardeno et al. [42] for the characterization of healthy helicopter blades, or by Poblete et al. [43] for piezoelectric sensors used in energy harvesting.

6.5. Uncertainty propagation

The uncertainty from the input parameters can be propagated to the model output using the sampled parameters from the distributions presented in Fig. 12, resulting in a model response with CIs. Fig. 13(a) illustrates the process of uncertainty propagation, using the distributions obtained for cell A as an example.

For the uncertainty propagation, first the temperature is selected; in Fig. 13(a), a temperature of 10 °C is used as an example. Then, the posterior PDFs corresponding to the selected temperature are defined. This can either be done using the samples obtained during the inference process or kernel density estimate based on these samples. Subsequently, the pole-residue model is evaluated using the samples drawn from the posterior distribution. From the evaluated FRFs, the 2.5% and 97.5% percentiles are computed at each frequency point to construct the CIs for the model response, which are shown in gray in Fig. 13(a).

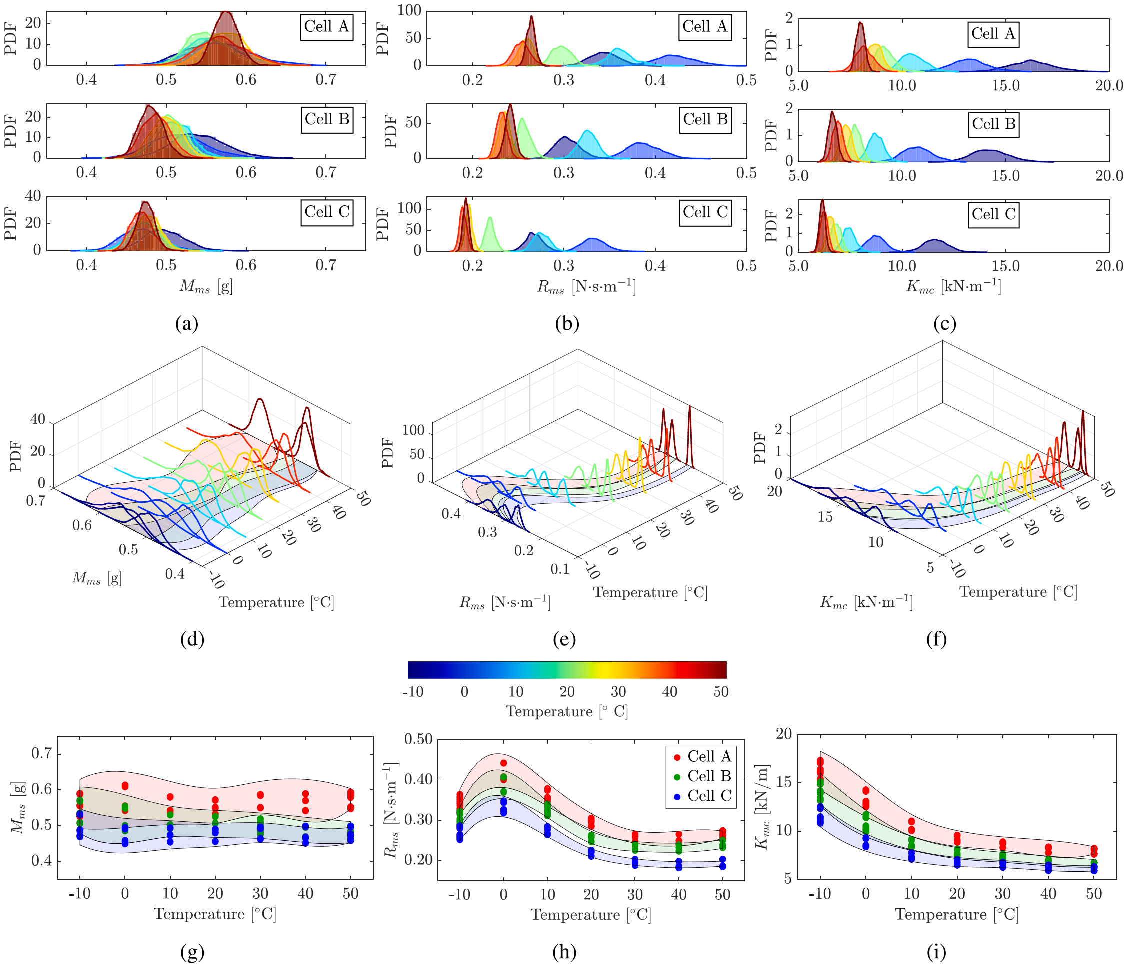

Fig. 12. Results for the Bayesian inference process: 2D histograms of the sampled posterior PDFs for cells A, B and C for: (a) M_{ms}, (b) R_{ms}, (c) K_{mc}; and 3D visualization of the sampled distributions for cells A, B and C: (d) M_{ms}, (e) R_{ms}, (f) K_{mc}. The color bar indicates the temperature for the 2D and 3D histograms from −10 °C to 50 °C. 2D representation of the distributions with the 95% CIs for (g) M_{ms}, (h) R_{ms}, (i) K_{mc}. The dots indicate the experimental samples and the shaded areas represent the 95% CIs (obtained from the 2.5% and 97.5% percentiles).

Figs. 13(b) and 13(c) present CIs for the phase and magnitude for the estimated FRF using the pole-residue model and compares it to the experimental results from −10 to 50 °C. Given the effect of the temperature on reducing the damping of the loudspeaker at higher temperatures, note that the CIs for −10 °C is wider when compared to the one obtained using the posterior distributions for 50 °C. In all three cases, the CIs generated by the model encompass the experimental data in a -3 dB range from the resonance peak. Outside of this region, the model predictions deviate from the experimental observations, especially at higher frequencies for the experiments at 50 °C and lower frequencies for the experiments at −10 °C. In the former, it is possible to note a possible mode of the electroacoustic absorber around 600 Hz, both by evaluating the amplitude and the phase of the frequency response function.

The CIs can also be evaluated in the acoustic domain of the system through the absorption coefficient of the EA, using Eq. (13). Fig. 13(d) presents the absorption coefficient determined using the numerical model and compares it with the experimental results. A good agreement is observed between the experimental data and the CIs near the resonance region of the model. This can be attributed to the accurate fit of the pole-residue model around the -3 dB point of the resonance. Outside the resonance region, the numerical model underestimates the absorption coefficient, as it does not account for additional mechanisms through which the EA may dissipate acoustic energy, such as cavity modes in the back box of the loudspeaker. Despite this limitation, the model remains suitable for predicting the absorption coefficient in the region $\alpha \geq \alpha_{th}$, which corresponds to the condition where the total sound intensity on the loudspeaker diaphragm is less than twice the intensity of the normally incident wave.

Table 5
Quantification of uncertainty on the Thiele-Small parameters for temperature range from −10 °C to 50 °C for EAs A, B, and C.

Loudspeaker	Parameter	Metric	Temperature [°C]						
			−10	0	10	20	30	40	50
A	M_{ms} [g]	Mean	0.558	0.569	0.559	0.552	0.575	0.569	0.575
		CV [%]	6.30	6.76	5.60	4.59	4.14	5.28	2.54
		2.5% percentile	0.492	0.495	0.503	0.506	0.530	0.512	0.547
		97.5% percentile	0.629	0.651	0.624	0.605	0.624	0.630	0.604
	R_{ms} [Ns/m]	Mean	0.344	0.422	0.362	0.297	0.259	0.254	0.264
		CV [%]	4.67	5.03	3.98	3.50	2.99	3.65	1.75
		2.5% percentile	0.314	0.382	0.336	0.278	0.244	0.237	0.255
		97.5% percentile	0.377	0.465	0.393	0.317	0.274	0.273	0.273
	K_{mc} [kN/m]	Mean	16.2	13.2	10.5	9.2	8.7	8.2	8.0
		CV [%]	6.29	6.69	5.56	4.57	4.11	5.25	2.51
		2.5% percentile	14.3	11.5	9.5	8.4	8.0	7.4	7.6
		97.5% percentile	18.3	15.1	11.7	10.1	9.4	9.1	8.4
B	M_{ms} [g]	Mean	0.540	0.515	0.511	0.505	0.500	0.487	0.481
		CV [%]	6.00	6.57	4.26	3.84	3.72	3.71	3.16
		2.5% percentile	0.480	0.451	0.469	0.467	0.464	0.453	0.453
		97.5% percentile	0.608	0.586	0.555	0.543	0.536	0.524	0.512
	R_{ms} [Ns/m]	Mean	0.304	0.387	0.326	0.256	0.235	0.232	0.241
		CV [%]	4.39	4.64	3.08	2.95	2.60	2.52	2.22
		2.5% percentile	0.280	0.354	0.307	0.243	0.223	0.221	0.230
		97.5% percentile	0.332	0.424	0.346	0.273	0.248	0.244	0.252
	K_{mc} [kN/m]	Mean	14.2	10.7	8.7	7.7	7.3	6.9	6.7
		CV [%]	5.94	6.49	4.22	3.79	3.67	3.66	3.13
		2.5% percentile	12.7	9.4	8.0	7.2	6.8	6.4	6.3
		97.5% percentile	16.0	12.2	9.5	8.3	7.8	7.4	7.1
C	M_{ms} [g]	Mean	0.496	0.468	0.473	0.474	0.479	0.469	0.474
		CV [%]	5.13	5.28	4.19	3.60	2.98	2.84	2.30
		2.5% percentile	0.446	0.424	0.435	0.442	0.453	0.444	0.453
		97.5% percentile	0.547	0.521	0.514	0.507	0.508	0.496	0.496
	R_{ms} [Ns/m]	Mean	0.268	0.333	0.275	0.219	0.196	0.190	0.193
		CV [%]	3.55	3.90	3.15	2.36	2.07	2.04	1.64
		2.5% percentile	0.250	0.309	0.260	0.209	0.188	0.182	0.186
		97.5% percentile	0.287	0.360	0.293	0.230	0.205	0.197	0.199
	K_{mc} [kN/m]	Mean	11.6	8.8	7.4	6.8	6.6	6.2	6.2
		CV [%]	5.07	5.22	4.18	3.57	2.97	2.81	2.30
		2.5% percentile	10.5	7.9	6.9	6.3	6.2	5.9	5.9
		97.5% percentile	12.8	9.7	8.1	7.3	7.0	6.6	6.4

7. Conclusions

This study investigates the impact of temperature variations on the mechanical properties of loudspeaker materials used in electroacoustic absorbers (EAs). The work focuses on quantifying the uncertainties in the Thiele-Small parameters and propagating them to the frequency response function and absorption coefficient of the EAs.

The results for the Thiele-Small parameters indicate that the system's natural frequency exhibits a nonlinear relationship with temperature, showing small variations of up to 8.1% at higher temperatures (50 °C) and significantly larger changes of up to 31.9% at lower temperatures (−10 °C), compared to the reference value at 20 °C. By identifying the Thiele-Small parameters from experimental frequency response functions, it was observed that the equivalent mass of the loudspeaker remains approximately constant across the studied temperature range. In contrast, the stiffness and resistance display nonlinear trends, with a noticeable transition around 20 °C. This behavior is consistent with the viscoelastic nature of the materials used in loudspeaker construction.

An uncertainty analysis was performed via the Bayesian inference framework using both the classical Metropolis–Hastings sampler and the affine invariant ensemble sampling (AIES) algorithms. The Metropolis–Hastings sampler exhibited persistent convergence difficulties when sampling the coupled parameters M_{ms} and K_{mc}, leading to under-dispersed posterior, biased confidence intervals, and extensive hyperparameter tuning with little improvement. By contrast, the AIES handled the strong posterior correlations through its stretch-move updates, and produced reliable confidence intervals for the Thiele-Small parameters.

Uncertainty was propagated using the AIES-derived posteriors, producing predictive intervals for the FRF and absorption coefficient that fully encompassed the experimental data. By using not just fixed values but full distributions for the Thiele-Small parameters, it becomes possible to make more informed predictions, such as defining reliable margins for the frequency response function and absorption coefficient of the EA.

Further studies are recommended on the application of the hierarchical Bayesian framework to the identification of individual cells. Given that the cells exhibit similar property distributions, these distributions could be linked through a higher-level distribution

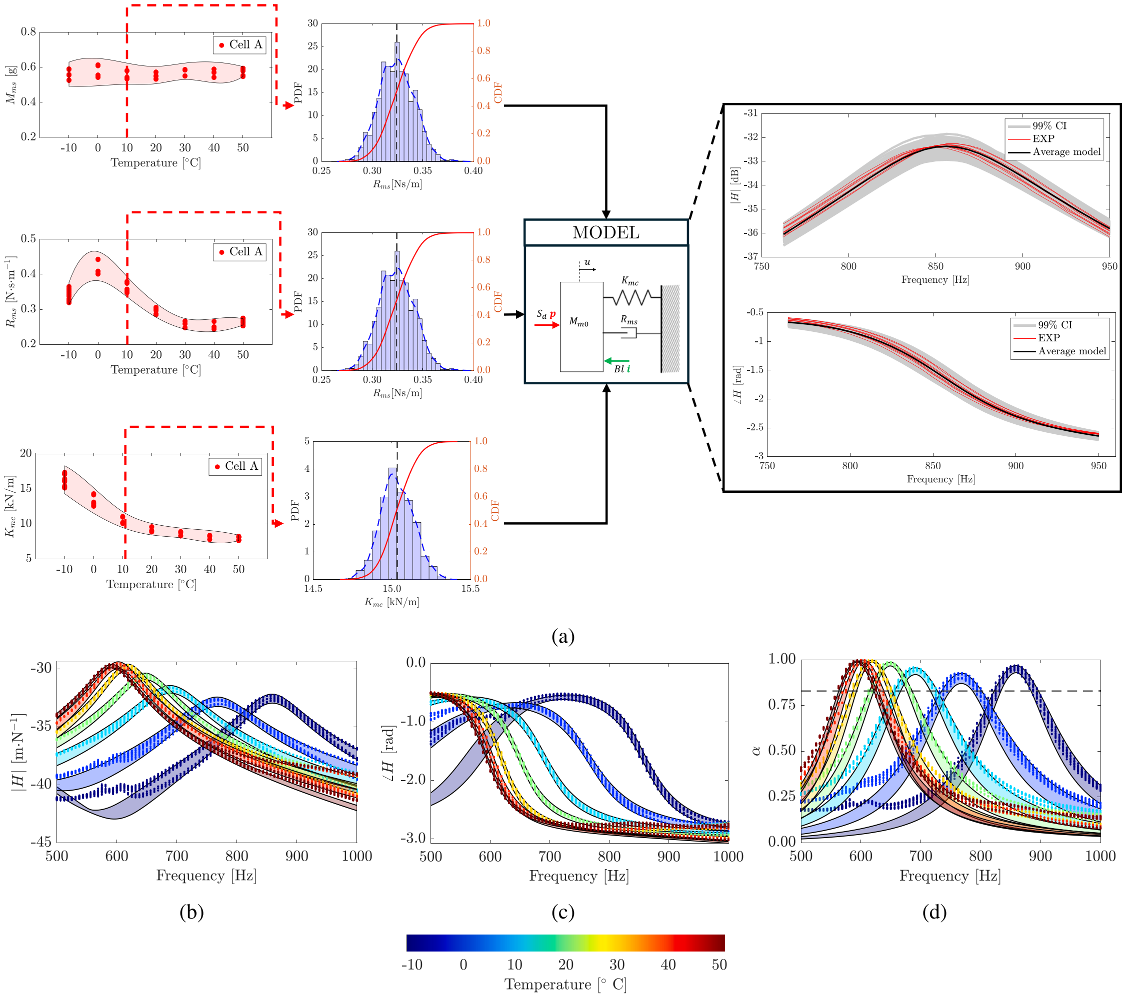

(a)

(b) (c) (d)

Fig. 13. Illustration of the process of uncertainty propagation applied to cell A. (a) The posterior distributions for M_{ms}, R_{ms}, and K_{mc} and be evaluated at a given temperature and then used to generate FRFs through the pole-residue model with CIs. In the histograms, the colors represent: Sampled data (▨), Kernel Density Estimate (KDE) (- -) and Cumulative Density Function (CDF) (▬). The CIs can be evaluated for the (b) magnitude of the FRF, (c) phase of the FRF, and (d) absorption coefficient with the dashed horizontal line indicating $\alpha_{th} = 1 - (\sqrt{2} - 1)^2$. In figures b–d, the solid regions represent the CI and the dots the experimental samples. The colors from blue to red represent the different temperatures from −10 °C to 50 °C.

parameterized by hyperparameters. Each cell can be treated as a domain within a population and used to infer properties both at the domain level and at the population level. From a practical standpoint, this approach would enable inference of the properties of unknown cells based on limited information, for example, values evaluated at a reference temperature, potentially reducing the number of tests required for new cells.

CRediT authorship contribution statement

Leonardo Ferreira: Writing – original draft, Software, Methodology, Investigation, Data curation, Conceptualization. **Rafael Teloli:** Writing – review & editing, Formal analysis. **Emanuele De Bono:** Writing – review & editing, Validation. **Morvan Ouisse:** Writing – review & editing, Supervision, Funding acquisition.

Declaration of competing interest

The authors declare that they have no known competing financial interests or personal relationships that could have appeared to influence the work reported in this paper.

Acknowledgments

This work has been supported by the EUR EIPHI Project (contract ANR-17-EURE-0002) and Bourgogne-Franche-Comté Region. The authors would like to acknowledge Stani Carbillet and the AMETISTE platform for the support.

Data availability

Data will be made available on request.

References

[1] X. Ma, Z. Su, Development of acoustic liner in aero engine: A review, Sci. China Technol. Sci. 63 (12) (2020) 2491–2504.
[2] L. Lu, K.-L. Yin, R.C. de Lamare, Z. Zheng, Y. Yu, X. Yang, B. Chen, A survey on active noise control in the past decade—Part I: linear systems, Signal Process. 183 (2021) 108039.
[3] H.F. Olson, E.G. May, Electronic sound absorber, J. Acoust. Soc. Am. 25 (6) (1953) 1130–1136.
[4] E. Rivet, S. Karkar, H. Lissek, Broadband low-frequency electroacoustic absorbers through hybrid sensor-/shunt-based impedance control, IEEE Trans. Control Syst. Technol. 25 (1) (2017) 63–72.
[5] K. Billon, M. Gillet, E. Salze, M. Volery, E. De Bono, M. Ouisse, H. Lissek, M. Collet, J. Mardjono, Smart acoustic lining for UHBR technologies engine: From the design of an electroacoustic metasurface to experimental characterization under flow, in: Active and Passive Smart Structures and Integrated Systems XVII, 12483, SPIE, 2023, pp. 390–396, http://dx.doi.org/10.1117/12.2658519.
[6] K. Billon, E. De Bono, M. Perez, E. Salze, G. Matten, M. Gillet, M. Ouisse, M. Volery, H. Lissek, J. Mardjono, M. Collet, In flow acoustic characterisation of a 2D active liner with local and non local strategies., Appl. Acoust. 191 (2022) 108655.
[7] E. De Bono, M. Collet, M. Ouisse, The advection boundary law in absence of mean flow: passivity, nonreciprocity and enhanced noise transmission attenuation, J. Sound Vib. 590 (2024) 118603.
[8] E. De Bono, M. Morell, M. Collet, E. Gourdon, A. Ture Savadkoohi, M. Ouisse, C.H. Lamarque, Model-inversion control to enforce tunable duffing-like acoustical response on an electroacoustic resonator at low excitation levels, J. Sound Vib. 570 (2024) 118070.
[9] M. Volery, X. Guo, H. Lissek, Robust direct acoustic impedance control using two microphones for mixed feedforward-feedback controller, Acta Acust. 7 (2023) 2.
[10] E. De Bono, M. Collet, M. Ouisse, E. Salze, M. Volery, H. Lissek, J. Mardjono, The advection boundary law in presence of mean flow and plane wave excitation: passivity, nonreciprocity and enhanced noise transmission attenuation, J. Sound Vib. 618 (2025) 119293.
[11] E. De Bono, M. Collet, K. Billon, E. Salze, H. Lissek, M. Volery, M. Ouisse, J. Marjono, Smart acoustic lining for UHBR technologies engine part 2: Acoustic treatment at the intake of a scaled turbofan nacelle, in: 30th AIAA/CEAS Aeroacoustics Conference (2024), 2024, arXiv:https://arc.aiaa.org/doi/pdf/10.2514/6.2024-3304. http://dx.doi.org/10.2514/6.2024-3304.
[12] E. De Bono, E. Salze, M. Collet, M. Gillet, M. Ouisse, M. Volery, H. Lissek, J. Mardjono, Experimental assessment of a programmable electroacoustic liner in a representative turbofan facility, Appl. Acoust. 240 (2025) 110896.
[13] L. Ferreira, R.d.O. Teloli, E. de Bono, M. Ouisse, Effect of the temperature on the impedance control of pressure-based, current-driven electroacoustic absorbers: addressing the loss of passivity using a viscoelastic material model, J. Sound Vib. 621 (2026) 119468.
[14] A. Novak, Modeling viscoelastic properties of loudspeaker suspensions using fractional derivatives, J. Audio Eng. Soc. 64 (1/2) (2016) 35–44.
[15] M. Rousseau, J. Vanderkooy, Visco-elastic aspects of loudspeaker drivers, in: 118th Convention of the Audio Engineering Society, AES, Barcelona, Spain, 2005, https://aes2.org/publications/elibrary-page/?id=13240.
[16] C.A. Henricksen, Heat-transfer mechanisms in loudspeakers: Analysis, measurement, and design, J. Audio Eng. Soc. 35 (1987) 778–791.
[17] P.J. Chapman, Thermal simulation of loudspeakers, J. Audio Eng. Soc. (4667) (1998).
[18] B. Maillou, P. Lotton, A. Novak, L. Simon, Modelling nonlinear viscoelastic behaviours of loudspeaker suspensions-like structures, J. Sound Vib. 416 (2018) 213–223.
[19] S. Laurin, K. Reichard, Determining manufacture variation in loudspeakers through measurement of thiele/small parameters, in: Audio Engineering Society - 125th Audio Engineering Society Convention 2008, 2008, pp. 854–857.
[20] B. Chojnacki, Dispersion influence of electroacoustic transducer parameters in the design process of miniature loudspeaker arrays and omnidirectional sound sources, Sensors 24 (15) (2024) 4958.
[21] C.M. Bellini, A. Farina, Loudspeakers performance variance due to components and assembly process, in: Proceedings of the 142nd Audio Engineering Society (AES) Convention, Audio Engineering Society, Berlin, Germany, 2017, pp. P4–1, AES Convention Paper 9714.
[22] J. Goodman, J. Weare, Ensemble samplers with affine invariance, Commun. Appl. Math. Comput. Sci. 5 (1) (2010) 65–80.
[23] A. International, Standard Test Method for Impedance and Absorption of Acoustical Materials Using a Tube, Two Microphones and a Digital Frequency Analysis System (E1050-24), ASTM International, West Conshohocken, PA, USA, 2024, Published May 1, 2024.
[24] R. Boulandet, H. Lissek, Toward broadband electroacoustic resonators through optimized feedback control strategies, J. Sound Vib. 333 (20) (2014) 4810–4825.
[25] M. Malléjac, M. Volery, H. Lissek, R. Fleury, Active control of electroacoustic resonators in the audible regime: Control strategies and airborne applications, Npj Acoust. 1 (1) (2025) 4.
[26] K. Billon, E. De Bono, M. Perez, E. Salze, G. Matten, M. Gillet, M. Ouisse, M. Volery, H. Lissek, J. Mardjono, M. Collet, In flow acoustic characterisation of a 2D active liner with local and non local strategies., Appl. Acoust. 191 (2022) 108655.
[27] B. Peeters, P. Guillaume, H. Van der Auweraer, B. Cauberghe, P. Verboven, J. Leuridan, Automotive and aerospace applications of the PolyMAX modal parameter estimation method, Proc. IMAC 22 Int. Modal Anal. Conf. (2004).
[28] K. Jaboviste, E. Sadoulet-Reboul, R.O. Teloli, G. Chevallier, Characterizing the nonlinear behavior of viscoelastic materials: A Bayesian approach combining oberst beam experiments and digital-twin simulations, Mech. Syst. Signal Process. 208 (2024) 110978.
[29] L.d.S. Ferreira, R.d.O. Teloli, S. da Silva, E. Figueiredo, I.D. Moldovan, N. Maia, C.A. Cimini, Bayesian calibration for Lamb wave propagation on a composite plate using a machine learning surrogate model, Mech. Syst. Signal Process. 208 (2024) 111011.
[30] R. da S Raqueti, R. de O Teloli, S. da Silva, P. Bussetta, A. CunhaJr, On the use of stochastic Bouc–Wen model for simulating viscoelastic internal variables from a finite element approximation of steady-rolling tire, J. Vib. Control 29 (19–20) (2023) 4799–4813.
[31] E. Simoen, G.D. Roeck, G. Lombaert, Dealing with uncertainty in model updating for damage assessment: A review, Mech. Syst. Signal Process. 56–57 (2015) 123–149.
[32] R. Allison, J. Dunkley, Comparison of sampling techniques for Bayesian parameter estimation, Mon. Not. R. Astron. Soc. 437 (4) (2014) 3918–3928.
[33] A. Lye, A. Cicirello, E. Patelli, A review of stochastic sampling methods for Bayesian inference problems, in: 29th European Safety and Reliability Conference, ESREL 2019, 2019, pp. 1866–1873.

[34] J. Zhang, J. Yin, R. Wang, Basic framework and main methods of uncertainty quantification, Math. Probl. Eng. 2020 (1) (2020) 6068203.
[35] A. Lye, A. Cicirello, E. Patelli, Sampling methods for solving Bayesian model updating problems: A tutorial, Mech. Syst. Signal Process. 159 (2021) 107760.
[36] Y. Huang, J.L. Beck, H. Li, Bayesian system identification based on hierarchical sparse Bayesian learning and gibbs sampling with application to structural damage assessment, Comput. Methods Appl. Mech. Engrg. 318 (2017) 382–411.
[37] J.L. Beck, S.-K. Au, Bayesian updating of structural models and reliability using Markov chain Monte Carlo simulation, J. Eng. Mech. 128 (4) (2002) 380–391.
[38] J. Zhang, Modern Monte Carlo methods for efficient uncertainty quantification and propagation: A survey, WIREs Comput. Stat. 13 (5) (2021) e1539.
[39] X. Meng, J.L. Beck, Y. Huang, H. Li, Adaptive meta-learning stochastic gradient Hamiltonian Monte Carlo simulation for Bayesian updating of structural dynamic models, Comput. Methods Appl. Mech. Engrg. 437 (2025) 117753.
[40] E. De Bono, M. Collet, G. Matten, S. Karkar, H. Lissek, M. Ouisse, K. Billon, T. Laurence, M. Volery, Effect of time delay on the impedance control of a pressure-based, current-driven electroacoustic absorber, J. Sound Vib. 537 (2022) 117201.
[41] A. Gelman, D.B. Rubin, Inference from iterative simulation using multiple sequences, Statist. Sci. 7 (1992) 457–472.
[42] T.A. Dardeno, K. Worden, N. Dervilis, R.S. Mills, L.A. Bull, On the hierarchical Bayesian modelling of frequency response functions, Mech. Syst. Signal Process. 208 (2024) 111072.
[43] A. Poblete, R.O. Ruiz, G. Jia, Hierarchical Bayesian approach for model parameter updating in piezoelectric energy harvesters, Mech. Syst. Signal Process. 172 (2022) 108942.